Spin state and spectroscopic modes of multiferroic $BiFeO_3$

Randy S. Fishman,[1] Jason T. Haraldsen,[2,3] Nobuo Furukawa,[4] and Shin Miyahara[5]

[1]*Materials Science and Technology Division, Oak Ridge National Laboratory, Oak Ridge, Tennessee 37831, USA*
[2]*Theoretical Division, Los Alamos National Laboratory, Los Alamos, New Mexico 87545, USA*
[3]*Center for Integrated Nanotechnologies, Los Alamos National Laboratory, Los Alamos, New Mexico 87545, USA*
[4]*Department of Physics and Mathematics, Aoyama Gakuin University, Sagamihara, Kanagawa 229-8558, Japan*
[5]*Asia Pacific Center for Theoretical Physics, Pohang University of Science and Technology, Pohang, Gyeongbuk, 790-784, Korea*

(Received 19 February 2013; published 19 April 2013)

Spectroscopic modes provide the most sensitive probe of the very weak interactions responsible for the properties of the long-wavelength cycloid in the multiferroic phase of $BiFeO_3$ below $T_N \approx 640$ K. Three of the four modes measured by terahertz (THz) and Raman spectroscopies were recently identified using a simple microscopic model. While a Dzyaloshinskii-Moriya (DM) interaction D along $[-1,2,-1]$ induces a cycloid with wave vector $(2\pi/a)(0.5+\delta,0.5,0.5-\delta)$ ($\delta \approx 0.0045$), easy-axis anisotropy K along the $[1,1,1]$ direction of the electric polarization $\mathbf{P}$ induces higher harmonics of the cycloid, which split the Ψ_1 modes at 2.49 and 2.67 meV and activate the Φ_2 mode at 3.38 meV. However, that model could not explain the observed low-frequency mode at about 2.17 meV. We now demonstrate that an additional DM interaction D' along $[1,1,1]$ not only produces the observed weak ferromagnetic moment of the high-field phase above 18 T but also activates the spectroscopic matrix elements of the nearly degenerate, low-frequency Ψ_0 and Φ_1 modes, although their scattering intensities remain extremely weak. Even in the absence of easy-axis anisotropy, D' produces cycloidal harmonics that split Ψ_1 and activate Φ_2. However, the observed mode frequencies and selection rules require that both D' and K are nonzero. This work also resolves an earlier disagreement between spectroscopic and inelastic neutron-scattering measurements.

DOI: 10.1103/PhysRevB.87.134416 PACS number(s): 75.25.−j, 75.30.Ds, 78.30.−j, 75.50.Ee

I. INTRODUCTION

As the only known room-temperature multiferroic, $BiFeO_3$ continues to attract a great deal of attention. Multiferroic materials offer the tantalizing prospect of controlling magnetic properties with electric fields or electric polarizations with magnetic fields.[1] Although the ferroelectric transition temperature[2] $T_c \approx 1100$ K of $BiFeO_3$ is far higher than its Néel temperature[3–5] $T_N \approx 640$ K, the electric polarization $\mathbf{P}$ is enhanced by its coupling to the long-wavelength cycloid below T_N (Ref. 6). As a result, the magnetic domain distribution below T_N can be manipulated by an electric field.[4,5,7]

Before $BiFeO_3$ can be used in technological applications, however, it is essential to understand the microscopic mechanisms and interactions responsible for its magnetic behavior. At frequencies above a few meV up to about 70 meV, the spin-wave (SW) spectrum of $BiFeO_3$ has been used[8,9] to determine the nearest-neighbor and next-nearest-neighbor exchange interactions $J_1 \approx -4.5$ meV and $J_2 \approx -0.2$ meV between the $S = 5/2$ Fe^{3+} spins[10] on a pseudocubic lattice with lattice constant $a \approx 3.96$ Å. As shown in Fig. 1(a), J_1 is the antiferromagnetic (AF) interaction between spins on neighboring $(1,1,1)$ planes separated by $c = a/\sqrt{3}$ while J_2 is the AF interaction between neighboring spins on each hexagonal layer.

Below T_N, a long-wavelength cycloid with wave vector[3,11–13] $\mathbf{Q} = (2\pi/a)[0.5+\delta,0.5,0.5-\delta]$ ($\delta \approx 0.0045$) is produced by the Dzyaloshinskii-Moriya (DM) interaction $\mathbf{D} = D\mathbf{y}'$ along $\mathbf{y}' = [-1,2,-1]$ (all unit vectors are assumed normalized to 1). As shown in Fig. 1(b), the spins of the cycloid lie predominantly in the $(-1,2,-1)$ plane normal to $\mathbf{y}'$.

Whereas the high-frequency portion of the SW spectrum determines the Heisenberg exchange interactions, the low-frequency modes measured by terahertz[14,15] (THz) and Raman[16–18] spectroscopies can be used to determine the small microscopic interactions that control the cycloid. Four modes have been detected at frequencies[10] of 2.17, 2.49, 2.67, and 3.35 meV. By comparison, a model with the single DM interaction $\mathbf{D}$ produces only[19] a single spectroscopically active mode labeled Ψ_1 at about 2.37 meV.

A more realistic model[19,20] also contains the easy-axis anisotropy K along $\mathbf{z}' = [1,1,1]$, parallel to the electric polarization $\mathbf{P}$. When $K > 0$, Ψ_1 splits into two and Φ_2 at 3.38 meV is activated.[19] Although this model successfully described the upper three spectroscopic modes, with predicted frequencies very close to the measured frequencies, it failed to explain the low-frequency 2.17 meV mode. In addition, it provides conflicting estimates for K based on spectroscopic and inelastic neutron-scattering measurements.

Several authors[21–24] have examined the effects of another DM interaction $\mathbf{D}' = D'\mathbf{z}'$ between neighboring hexagonal layers. For a G-type AF, D' produces a weak ferromagnetic moment along $\mathbf{y}'$ due to the canting of the uniform moments on each hexagonal plane. The moment $\mathbf{M}_0 = 2\mu_B S_0 \mathbf{y}' \approx 0.03\mu_B \mathbf{y}'$ was subsequently observed in the metamagnetic phase[6,25] above 18 T. Below 18 T, D' was predicted[23] to induce an oscillatory component of the cycloid along $\mathbf{y}'$, which has recently been confirmed by neutron-scattering measurements.[26]

Based on a model that includes both D and D' in addition to the easy-axis anisotropy K, we evaluate the spin state and spectroscopic modes of $BiFeO_3$. Even when $K = 0$, D' induces higher harmonics of the cycloid that split Ψ_1 and activate Φ_2. More remarkably, D' activates Ψ_0 and Φ_1 at the cycloidal wave vector.

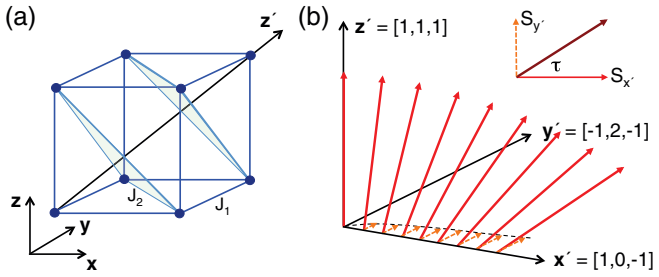

FIG. 1. (Color online) (a) The pseudocubic cell with exchange interactions J_1 and J_2 as well as the polarization direction $\mathbf{z}'$ cutting through two hexagonal planes. (b) For domain 1, a schematic of the spins along the x' axis showing their rotation about $\mathbf{y}'$. Due to the DM interaction $\mathbf{D}' = D'\mathbf{z}'$, spins rotate by τ about $\mathbf{z}'$ in the $x'y'$ plane.

We believe that these nearly degenerate modes are responsible for the low-frequency 2.17 meV peak observed in spectroscopy measurements. Although a model with $K = 0$ can produce four spectroscopic modes, the Ψ_1 selection rules are reversed and their mode frequencies are too small. Therefore, both D' and K are required to explain the experimental measurements. With $D' \approx 0.054$ meV, corresponding to the observed value[6,25] $S_0 = 0.015$, we estimate that $D \approx 0.11$ meV and $K \approx 0.0035$ meV, which also provide a good description of inelastic neutron-scattering measurements[9] below 5 meV.

This paper is divided into seven sections. Section II constructs the spin state of $BiFeO_3$. Section III evaluates the spin dynamics of that state, Sec. IV evaluates the spectroscopic modes of that state, and Sect. V discusses the selection rules for those modes. Section VI discusses the inelastic neutron-scattering spectrum for the low-frequency modes. Section VII contains a brief conclusion. Results for the SW intensities are provided in Appendix A. The polarization and magnetic matrix elements are provided in Appendix B.

II. SPIN STATE

With $\mathbf{P} = P\mathbf{z}'$, the three magnetic domains have cycloidal wave vectors $\mathbf{Q} = (2\pi/a)[0.5+\delta,0.5,0.5-\delta]$ (domain 1), $(2\pi/a)[0.5,0.5+\delta,0.5-\delta]$ (domain 2), or $(2\pi/a)[0.5+\delta,0.5-\delta,0.5]$ (domain 3). By contrast, the G-type AF stabilized by a magnetic field,[6,25] doping,[27] or in thin films[28] has wave vector $(2\pi/a)[0.5,0.5,0.5]$. In our discussion of the selection rules governing the spectroscopic modes in Sec. V, we will assume that all three domains are equally populated. Since the spin state and dynamics are the same for all three domains, we now concentrate on domain 1 with $\mathbf{x}' = [1,0,-1]$ and $\mathbf{y}' = [-1,2,-1]$, as shown in Fig. 1(b).

The spin state and SW excitations of $BiFeO_3$ are evaluated from the Hamiltonian

$$H = -J_1 \sum_{\langle i,j\rangle} \mathbf{S}_i \cdot \mathbf{S}_j - J_2 \sum_{\langle i,j\rangle'} \mathbf{S}_i \cdot \mathbf{S}_j - K \sum_i S_{iz'}^2 - D \sum_{\mathbf{R}_j = \mathbf{R}_i + a(\mathbf{x}-\mathbf{z})} \mathbf{y}' \cdot (\mathbf{S}_i \times \mathbf{S}_j) - D' \sum_{\mathbf{R}_j = \mathbf{R}_i + a\mathbf{x}, a\mathbf{y}, a\mathbf{z}} (-1)^{R_{iz'}/c}\, \mathbf{z}' \cdot (\mathbf{S}_i \times \mathbf{S}_j). \quad (1)$$

The first and second exchange terms contain sums $\langle i,j\rangle$ and $\langle i,j\rangle'$ over nearest and next-nearest neighbors on the pseudocubic lattice. The third term arises from the easy-axis anisotropy along $\mathbf{z}'$ and the fourth term from the DM interaction with $\mathbf{D} = D\mathbf{y}'$.

Compared to the model for $BiFeO_3$ introduced in Ref. 20 and studied in our earlier work,[19] H adds the DM interaction $\mathbf{D}' = D'\mathbf{z}'$. This term alternates in sign with increasing z': $(-1)^{R_{iz'}/c}$ changes sign from layer n to layer $n+1$ so the DM interaction $(-1)^{R_{iz'}/c}D'$ between layers n and $n+1$ has opposite sign to the DM interaction between layers $n+1$ and $n+2$. Hence, the DM interaction $\mathbf{D}'$ has the same wave vector $(2\pi/a)[0.5,0.5,0.5]$ as a G-type AF.

Because $\delta \approx 1/222$, a unit cell containing $M = 222$ sites within each of two neighboring (1,1,1) planes is used to characterize the distorted cycloid. In zero magnetic field, the cycloid can be expanded in odd harmonics[29,30] of the fundamental wave vector $\mathbf{Q}$ (even harmonics are also required in nonzero fields). If $S_{y'}(\mathbf{R})$ is proportional to $S_{x'}(\mathbf{R})$, then

$$S_{x'}(\mathbf{R}) = (-1)^{R_{z'}/c} \cos\tau \sqrt{S^2 - S_{z'}(\mathbf{R})^2} \times \mathrm{sgn}[\sin(2\pi\delta R_{x'}/a)], \quad (2)$$

$$S_{y'}(\mathbf{R}) = \sin\tau \sqrt{S^2 - S_{z'}(\mathbf{R})^2}\, \mathrm{sgn}[\sin(2\pi\delta R_{x'}/a)], \quad (3)$$

$$S_{z'}(\mathbf{R}) = (-1)^{R_{z'}/c} S \sum_{m=0}^{\infty} C_{2m+1} \cos[(2m+1)2\pi\delta R_{x'}/a]. \quad (4)$$

Odd-order coefficients C_{2m+1} in $S_{z'}(\mathbf{R})$ satisfy $\sum_{m=0}^{\infty} C_{2m+1} = 1$. Although $S_{y'}(\mathbf{R})$ [unlike $S_{x'}(\mathbf{R})$ and $S_{z'}(\mathbf{R})$] does not change sign from one layer to the next, the average value of $S_{y'}(\mathbf{R})$ vanishes and there is no net moment in any direction. The ratio $S_{y'}(\mathbf{R})/S_{x'}(\mathbf{R})$ has magnitude $\tan\tau\,\alpha\ |D'/J_1| \ll 1$. Although the cycloid remains coplanar for each hexagonal layer, the cycloidal planes rotate by 2τ from one layer to the next.

The parameters of the spin state are evaluated by minimizing the energy $E = \langle H\rangle$ in a unit cell $x'y'z'$ of dimensions $15\,000a \times a \times 2c$ containing two (1,1,1) layers. Open boundary conditions are employed along the x' direction. With the exchange interactions $J_1 = -4.5$ meV and $J_2 = -0.2$ meV fixed at the values required to describe the SW spectrum[8,9] at high frequencies, the four variational parameters are δ, τ, C_3, and C_5. A solution with $\delta = 1/222$ is obtained by varying the DM interaction D for fixed K. After minimizing the energy, we verify that the corresponding spin state provides at least a metastable minimum by checking that the classical forces on each spin vanish.

With a magnetic field oriented along $\mathbf{z}'$, the metamagnetic state observed[6,25] above 18 T can be written

$$\mathbf{S}_1 = S(\cos\theta\cos\phi, \cos\theta\sin\phi, \sin\theta), \quad (5)$$

$$\mathbf{S}_2 = S(-\cos\theta\cos\phi, \cos\theta\sin\phi, \sin\theta) \quad (6)$$

for $R_{z'} = 2mc$ and $(2m+1)c$, respectively. Extrapolating to zero field with $\theta = 0$, we obtain $\tan 2\phi = D'/J_1$. Hence, the

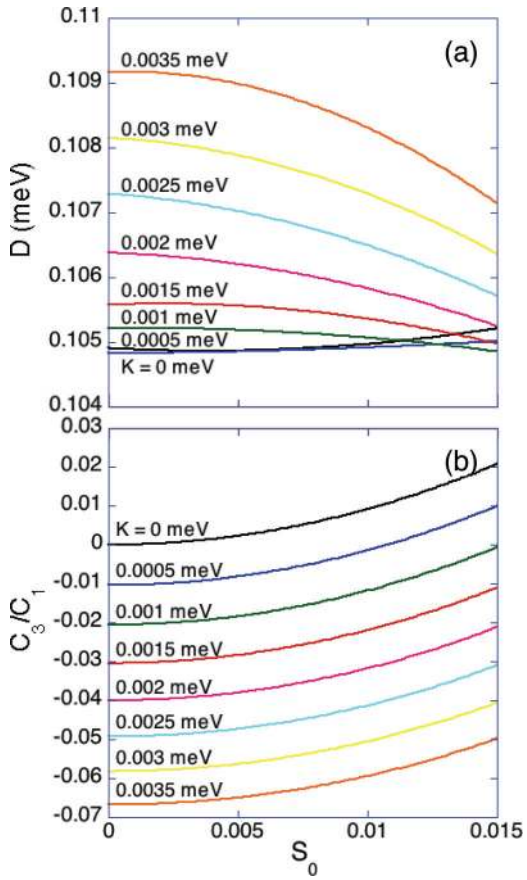

FIG. 2. (Color online) (a) The DM interaction D and (b) the ratio of harmonics C_3/C_1 versus S_0 for several values of K.

weak ferromagnetic moment of the metamagnetic phase is

$$M_0 = 2\mu_B S_0 = 2\mu_B S \sin\phi \approx \frac{\mu_B S D'}{J_1}, \tag{7}$$

independent of D, K, and J_2. Using $J_1 = -4.5$ meV and the experimental result[6,25] $S_0 = 0.015$, we estimate that $|D'| = 0.054$ meV, which is is slightly larger than the estimate $|D'| = 0.046$ meV provided in Ref. 24.

For the distorted cycloid given by Eqs. (2)–(4), it is straightforward to show that if $\delta \ll 1$, then $\tau \approx D'/2J_1$. Therefore, the *maximum* cycloidal spin $|S_{y'}(\mathbf{R})|$ equals the weak ferromagnetic spin S_0 of the metamagnetic phase. For the tilting angle, we estimate $\tau \approx 0.34^\circ$, a bit smaller than the recent neutron-scattering[26] estimate of $\sim 1^\circ$.

In Fig. 2(a), we plot the DM interaction D versus S_0 for several values of the anisotropy K ranging from 0 to 0.0035 meV. For $K = 0$ and 0.0005 meV, D increases slightly with S_0. But for $K \geqslant 0.001$ meV, D decreases with S_0. Nevertheless, the variation of D with S_0 is rather modest.

By contrast, the higher harmonics of the cycloid exhibit a much stronger variation with S_0. Figure 2(b) reveals that the ratio C_3/C_1 increases with S_0 for all K. Since $C_1 = 1 - \sum_{n=1} C_{2n+1}$ and $|C_5| \ll |C_3|$, $C_1 \approx 1 - C_3$ and $C_3/C_1 \approx C_3(1 + C_3)$. For $K = 0$ and $S_0 > 0$, $C_3 > 0$ and

$$\langle {S_{iz'}}^2 \rangle = \frac{1}{2}\sum_{n=0}(C_{2n+1})^2 \approx \frac{1}{2}(1 - 2C_3) < \frac{1}{2}. \tag{8}$$

Because the $\mathbf{D}'$ interaction energy is optimized when the spins lie in the $x'y'$ plane, higher harmonics favor the z' nodal regions of the cycloid. When S_0 is sufficiently small and $K > 0$, $C_3 < 0$ and $\langle S^2_{iz'} \rangle > 1/2$ so that higher harmonics favor the z' antinodal regions of the cycloid. Experimentally, the ratio of the neutron-scattering intensity from the third to the first harmonics is given by $(C_3/C_1)^2$.

Notice that the third (and higher) harmonics can vanish for nonzero S_0 and K. When $S_0 = 0.015$, $C_3 < 0$ when K is less than about 0.001 meV and $C_3 > 0$ when K is greater than about 0.001 meV. For $K \approx 0.001$ meV, the higher harmonics of the cycloid vanish and $\langle {S_{iz'}}^2 \rangle = 1/2$.

III. SW EXCITATIONS

The SW frequencies are calculated using the equations-of-motion technique for noncollinear spins outlined in Ref. 31. A unit cell containing $M = 222$ sites on each of two hexagonal layers is constructed to evaluate the $2M$ SW frequencies $\omega_n(\mathbf{q})$. SW intensities are obtained from the spin-spin correlation function defined by Eq. (A9) in Appendix A. In the absence of damping, the inelastic scattering cross section $S(\mathbf{q},\omega)$ can be expanded as sum over δfunctions at each frequency:

$$S(\mathbf{q},\omega) = \sum_{n,\alpha}[1 - (q_\alpha/q)^2]\delta(\omega - \omega_n(\mathbf{q}))S^{(n)}_{\alpha\alpha}(\mathbf{q}). \tag{9}$$

The amplitudes $S^{(n)}_{\alpha\alpha}(\mathbf{q})$ are evaluated using Eq. (A11).

For fixed $S_0 = 0.015$, the SW frequencies are plotted in Fig. 3 for $K = 0$, 0.001, and 0.002 meV. Although there are $2M$ modes for every wave vector $(2\pi/a)(0.5 + \eta, 0.5, 0.5 - \eta)$, plotted by the dashed lines, only a few of those modes have any significant intensity. Modes with intensity above an arbitrary cutoff are plotted in the dark lines.

When $K \approx 0.001$ meV in Fig. 3(b), the higher harmonics of the cycloid vanish and the SW frequencies are similar to those for $S_0 = 0$ and $K = 0$ discussed in Ref. 19. In the absence of harmonics, de Sousa and Moore[32] labeled the SW frequencies $\omega_n(mQ)$ $(n = 1$ or $2)$ of a one-dimensional cycloid at multiples

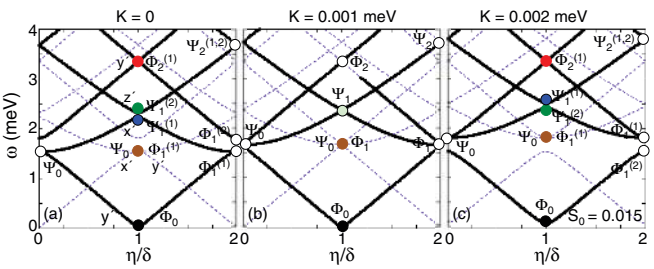

FIG. 3. (Color online) The SW modes of $BiFeO_3$ versus η/δ for wave vector $(2\pi/a)(0.5 + \eta, 0.5, 0.5 - \eta)$. The dashed lines show all possible excitations and the solid lines show only those modes with significant intensity above a threshold value. All three plots take $S_0 = 0.015$ and $D' = 0.054$ meV. Φ_0 (black dots) has a very large y' MR matrix element. The low-frequency mode (brown dots) has both Ψ_0 and $\Phi_1^{(1)}$ contributions with nonzero x' and y' MR matrix elements, respectively. Whereas $\Phi_2^{(1)}$ (red) has nonzero y' MR matrix element, $\Psi_1^{(1)}$ (blue) and $\Psi_1^{(2)}$ (green) have nonzero x' and z' matrix elements, respectively. The electromagnon (EM) mode with component y' coincides with $\Psi_1^{(1)}$.

m of the cycloidal wave vector $Q = 2\pi\delta/a$ as Φ_m and Ψ_m. Using an extended zone scheme and assuming that $|m|\delta \ll 1$, $\omega_n(mQ)$ can be approximated by $\Phi_m = \Phi_1|m|$ and $\Psi_m = \Phi_1\sqrt{1+m^2}$. These relations imply that $\Phi_1 = \Psi_0$, as seen in Fig. 3(b), and that the $\Phi_{\pm m}$ and $\Psi_{\pm m}$ modes cross without repulsion at the zone center $q = Q$ and zone boundary $q = 0$.

Whether produced by the tilt τ or by the anisotropy K, higher odd harmonics of the cycloid introduce higher even harmonics in the Hamiltonian H. A $2m\mathbf{Q}$ potential will split the $\Phi_{\pm m}$ and $\Psi_{\pm m}$ modes. As shown in Figs. 3(a) and 3(c), the new $m = 1$ eigenmodes are labeled $\Phi_1^{(1,2)}$ and $\Psi_1^{(1,2)}$. Notice that Ψ_0 and $\Phi_1^{(1)}$ are nearly degenerate for all K. Although too small to see in Fig. 3, even $\Phi_{\pm 2}$ are split by anharmonicity.

IV. SPECTROSCOPIC MODES

Because the wavelength of far-infrared light greatly exceeds atomic length scales, the SW modes measured by THz and Raman spectroscopies lie at the zone center $\mathbf{q} = \mathbf{Q}$ or $\eta = \delta$. A magnetic resonance (MR) mode has nonzero matrix element $\langle\delta|M_\alpha|0\rangle$, where $|0\rangle$ is the ground state and $|\delta\rangle$ is an excited state with a single magnon of wave vector $\mathbf{Q}$. An electromagnon (EM) mode has nonzero matrix element $\langle\delta|P_\alpha^{\rm ind}|0\rangle$ so that the induced polarization directly couples the ground state to the excited state.

In order to evaluate the MR and EM matrix elements, we must first express the magnetic moment $\mathbf{M}$ and induced polarization $\mathbf{P}^{\rm ind}$ operators in terms of the spin operators $\mathbf{S}_i$. The magnetic moment $\mathbf{M} = 2\mu_B \sum_{\mathbf{R}_i} \mathbf{S}_i$ contains a sum over the $2M$ unique sublattices. In $BiFeO_3$, the coupling between the cycloid and electric polarization is produced by the inverse DM mechanism[33–35] with induced polarization

$$\mathbf{P}^{\rm ind} = \lambda \sum_{\mathbf{R}_i,\mathbf{R}_j=\mathbf{R}_i+\mathbf{e}_{ij}} \{\mathbf{e}_{ij} \times (\mathbf{S}_i \times \mathbf{S}_j)\}, \qquad (10)$$

where the sum is restricted to the $2M$ sublattices using periodic boundary conditions. Within each (1,1,1) plane, $\mathbf{e}_{ij} = \sqrt{2}a\mathbf{x}'$ connects spins at sites $\mathbf{R}_i$ and $\mathbf{R}_j$. So if $\langle 0|\mathbf{S}_i \times \mathbf{S}_j|0\rangle$ points along $\mathbf{y}'$, then $\langle 0|\mathbf{P}^{\rm ind}|0\rangle$ points along $\mathbf{z}'$.

Expressions for the matrix elements $\langle\delta|M_\alpha|0\rangle$ and $\langle\delta|P_\alpha^{\rm ind}|0\rangle$ are provided in Appendix B. Although there is no simple relation between the MR matrix elements and the SW intensities, the MR and EM modes appear only at mode frequencies n with $S^{(n)}_{\alpha'\alpha'}(\delta) > 0$. Generally, Φ_n modes with $\langle\delta|M_{y'}|0\rangle \neq 0$ also have nonzero SW intensities $S^{(n)}_{x'x'}(\delta)$ and $S^{(n)}_{z'z'}(\delta)$. Hence, those modes excite spins within the $x'z'$ plane of the cycloid (neglecting its small tilt). On the other hand, Ψ_n modes with $\langle\delta|M_{x'}|0\rangle \neq 0$ or $\langle\delta|M_{z'}|0\rangle \neq 0$ also have $S^{(n)}_{y'y'}(\delta) > 0$. Hence, those modes excite spins out of the $x'z'$ plane.

Zone-center modes with nonzero MR matrix elements are indicated by the filled circles in Fig. 3. In addition to having an enormous SW intensity, the "zero"-frequency[36] Φ_0 mode has a very large MR matrix element (for $K = 0.0035$ meV and $S_0 = 0.015$, $|\langle\delta|M_{y'}|0\rangle| \approx 8400\mu_B$). The $2\mathbf{Q}$ potential splits the degenerate $\Psi_{\pm 1}$ modes into $\Psi_1^{(1)}$ ($\langle\delta|M_{x'}|0\rangle \neq 0$) and $\Psi_1^{(2)}$ ($\langle\delta|M_{z'}|0\rangle \neq 0$). The EM ($\langle\delta|P_{y'}^{\rm ind}|0\rangle \neq 0$) always coincides with $\Psi_1^{(1)}$. Similarly, the smaller $4\mathbf{Q}$ potential splits the $\Phi_{\pm 2}$ modes. Due to its hybridization with Φ_0, $\Phi_2^{(1)}$ becomes spectroscopically active with $\langle\delta|M_{y'}|0\rangle \neq 0$.

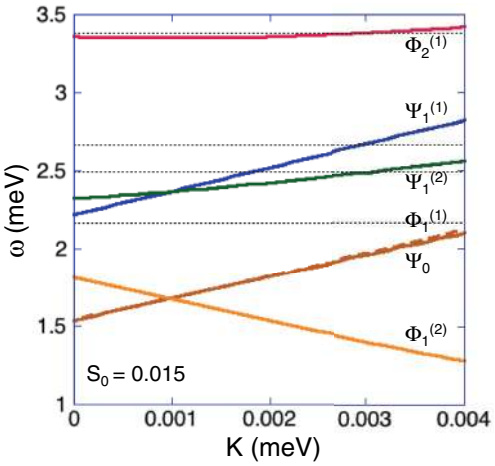

FIG. 4. (Color online) The evolution of the predicted modes with anisotropy K taking $S_0 = 0.015$ and $D' = 0.054$ meV. The horizontal dashed lines are the observed spectroscopic mode frequencies (Ref. 10).

The predicted mode frequencies are plotted versus anisotropy for $S_0 = 0.015$ in Fig. 4. Both $\Psi_1^{(1,2)}$ and $\Phi_1^{(1,2)}$ cross near $K = 0.001$ meV. At $\eta = \delta$, $\Phi_1^{(2)}$ has no SW intensity and is not spectroscopically active. But at $\eta = 0$, this mode is responsible for important features in the inelastic-scattering spectrum discussed in Sec. VI.

For $K = 0.0035$ meV, the mode frequencies are plotted versus S_0 in Fig. 5(a), where D and D' are evaluated in terms of S_0 for fixed $\delta = 1/222$. While the predicted spectroscopic mode frequencies decrease slightly with S_0, $\Phi_1^{(2)}$ slightly increases.

When $S_0 = 0$, the Ψ_0 and $\Phi_1^{(1)}$ modes at the zone center $\eta = \delta$ have no SW intensity and their MR matrix elements vanish. But when $S_0 > 0$, the DM interaction $\mathbf{D}'$ with wave vector $(2\pi/a)[0.5,0.5,0.5]$ hybridizes Ψ_0 with $\Psi_1^{(1,2)}$ and $\Phi_1^{(1)}$ with Φ_0. Consequently, their MR matrix elements become significant.

In Fig. 5(b), the mode frequencies and MR matrix elements of Ψ_0 and $\Phi_1^{(1)}$ are plotted versus S_0 together with the very small SW intensities of those modes for $K = 0.0035$ meV. As expected from perturbation theory, the matrix elements $\langle\delta|M_\alpha|0\rangle$ grow linearly with $S_0 \sim |D'/J_1|$. Moreover, they scale as the square root of the SW intensities $S_{\alpha'\alpha'}(\delta)$. Therefore, these modes are both spectroscopically and dynamically activated by the tilt of the cycloid. It is remarkable that the MR matrix elements of Ψ_0 and $\Phi_1^{(1)}$ become so large while their SW intensities remain extremely weak.

The dashed horizontal lines in Fig. 4 correspond to the four measured spectroscopic frequencies of $BiFeO_3$. We believe that the nearly degenerate Ψ_0 and $\Phi_1^{(1)}$ modes are responsible for the observed low-frequency peak at 2.17 meV. Recall that those two modes only appear when the cycloid is tilted away from the $x'z'$ plane by the DM interaction $\mathbf{D}'$ along $\mathbf{z}'$. The best overall fit to the observed mode spectrum is obtained with $K \approx 0.0035$ meV. Measured[10] and predicted mode frequencies are summarized in Table I.

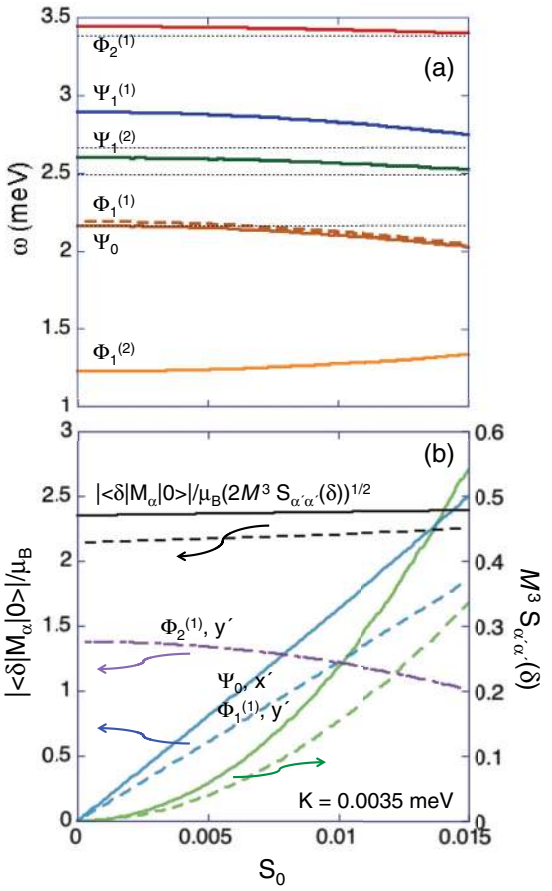

FIG. 5. (Color online) (a) The frequencies of the predicted modes versus S_0 for $K = 0.0035$ meV. Horizontal dashed lines are the measured spectroscopic frequencies (Ref. 10). (b) The MR matrix elements $|\langle\delta|M_\alpha|0\rangle|/\mu_B$ for Ψ_0 (solid) and $\Phi_1^{(1)}$ (dashed) versus S_0 for $K = 0.0035$ meV. Also plotted are the intensities $M^3 S_{\alpha'\alpha'}(\delta)$ of those modes ($\alpha' = y'$ for $\alpha = x'$ and $\alpha' = x'$ or z' for $\alpha = y'$) with $M = 222$. The normalized matrix element $|\langle\delta|M_\alpha|0\rangle|/\mu_B S_{\alpha'\alpha'}(\delta)^{1/2}$ is independent of S_0. The dash-dotted curve plots the MR matrix element for $\Phi_2^{(1)}$ with $\alpha = y'$.

With $S_0 = 0.015$ and $K = 0.0035$ meV, the harmonics of the cycloid have the ratio $C_3/C_1 = -0.050$ or $(C_1/C_3)^2 = 400$. Elastic neutron-scattering[11] and NMR measurements[37] indicate that $(C_1/C_3)^2$ is 500 and 25, respectively. However, the NMR measurement may overestimate the third harmonic due to the high ^{57}Fe isotope content of the sample.[38] Our estimate for $(C_3/C_1)^2$ is in very good agreement with the elastic neutron-scattering result.

TABLE I. Spectroscopic frequencies, matrix elements, and intensities.

	$\Psi_0/\Phi_1^{(1)}$	$\Psi_1^{(2)}$	$\Psi_1^{(1)}$	$\Phi_2^{(1)}$
Measured ω (meV)	2.17	2.49	2.67	3.38
Predicted ω (meV)	2.03/2.05	2.53	2.75	3.40
MR index α	x'/y'	z'	x'	y'
$\lvert\langle\delta\lvert M_\alpha\rvert 0\rangle\rvert/\mu_B$	2.50/1.86	3.96	4.59	1.01
$\lvert\langle\delta\lvert P_{y'}\rvert 0\rangle\rvert/\lambda$	0	0	12.2	0
Intensity index α'	$y'/x', z'$	y'	y'	x', z'
$S_{\alpha'\alpha'}(\delta)$	$4.94\times10^{-8}/3.05\times10^{-8}$	19.7	18.1	5.43,2.35
$I(\mathbf{h}_1)/\mu_B^2$	4.75	0	10.54	0.51
$I(\mathbf{h}_2)/\mu_B^2$	1.58	10.47	3.51	0.17

V. SELECTION RULES

We now consider the selection rules for the THz modes[14,15] for a sample with the single polarization domain $\mathbf{P} = P\mathbf{z}'$, where $\mathbf{z}' = [1,1,1]$. As mentioned in Sec. II, the three possible magnetic domains have wave vectors $(2\pi/a)(0.5+\delta,0.5,0.5-\delta)$, $(2\pi/a)(0.5,0.5+\delta,0.5-\delta)$, and $(2\pi/a)(0.5+\delta,0.5-\delta,0.5)$. Since these domains have the same energy, we expect them to be equally populated. The mode spectrum was measured for crossed fields $\mathbf{h}_1 = [1,-1,0]$ and $\mathbf{h}_2 = [1,1,0]$.

To predict the selection rules for $BiFeO_3$, $\mathbf{h}_1$ and $\mathbf{h}_2$ are expressed in terms of the cycloidal unit vectors $\mathbf{x}'$, $\mathbf{y}'$, and $\mathbf{z}'$ as

$$\mathbf{h}_1 = (\mathbf{x}' - \sqrt{3}\mathbf{y}')/2,$$
$$\mathbf{h}_2 = \mathbf{x}'/2 + \sqrt{3}\mathbf{y}'/6 + \sqrt{2/3}\mathbf{z}' \quad (11)$$

in domain 1 with $\mathbf{x}' = [1,0,-1]$ and $\mathbf{y}' = [-1,2,-1]$;

$$\mathbf{h}_1 = -(\mathbf{x}' + \sqrt{3}\mathbf{y}')/2,$$
$$\mathbf{h}_2 = \mathbf{x}'/2 - \sqrt{3}\mathbf{y}'/6 + \sqrt{2/3}\mathbf{z}' \quad (12)$$

in domain 2 with $\mathbf{x}' = [0,1,-1]$ and $\mathbf{y}' = [-2,1,1]$; and

$$\mathbf{h}_1 = \mathbf{x}',$$
$$\mathbf{h}_2 = (\mathbf{y}' + \sqrt{2}\mathbf{z}')/\sqrt{3} \quad (13)$$

in domain 3 with $\mathbf{x}' = [1,-1,0]$ and $\mathbf{y}' = [1,1,-2]$. Although the following discussion assumes that all three domains are equally populated, our qualitative conclusions remain unchanged even if one or two domain populations dominate the sample.

The spectroscopic intensity for any mode is given by[39]

$$I(\mathbf{h}) = \sum_\alpha h_\alpha^2 \,|\langle\delta|M_\alpha|0\rangle|^2. \quad (14)$$

Averaging over the three domains, we find

$$I(\mathbf{h}_1) = \tfrac{1}{2}\{|\langle\delta|M_{x'}|0\rangle|^2 + |\langle\delta|M_{y'}|0\rangle|^2\}, \quad (15)$$

$$I(\mathbf{h}_2) = \tfrac{1}{6}\{|\langle\delta|M_{x'}|0\rangle|^2 + |\langle\delta|M_{y'}|0\rangle|^2\} + \tfrac{2}{3}|\langle\delta|M_{z'}|0\rangle|^2. \quad (16)$$

For $\langle\delta|M_\alpha|0\rangle \neq 0$, $I(\mathbf{h}_1)/I(\mathbf{h}_2) = 3$ for any mode (such as $\Phi_2^{(1)}$, $\Psi_1^{(1)}$, $\Psi^{(0)}$, and $\Phi_1^{(1)}$) with $\alpha = x'$ or y' while $I(\mathbf{h}_1)/I(\mathbf{h}_2) = 0$ for any mode (such as $\Psi_1^{(2)}$) with $\alpha = z'$.

While $\Psi_1^{(1)}$ ($\langle\delta|M_{x'}|0\rangle \neq 0$) and $\Phi_2^{(1)}$ ($\langle\delta|M_{y'}|0\rangle \neq 0$) should appear in both fields $\mathbf{h}_1$ and $\mathbf{h}_2$, $\Psi_1^{(2)}$ ($\langle\delta|M_{z'}|0\rangle \neq 0$) should appear only in field $\mathbf{h}_2$, which contains a $\mathbf{z}'$ component. This agrees with the selection rule observed by Talbayev *et al.*[14] But Nagel *et al.*[15] recently found that $\Psi_1^{(2)}$ survives in field $\mathbf{h}_1$, albeit with $I(\mathbf{h}_1)/I(\mathbf{h}_2) = 0.11$. Notice that the position of $\Psi_1^{(1)}$ above $\Psi_1^{(2)}$ requires that $K > 0.001$ meV. Therefore, both nonzero K and S_0 are required to explain the spectroscopic frequencies and selection rules.

Whereas Talbayev *et al.*[14] found that the low-frequency mode appears only in field $\mathbf{h}_1$, our model indicates that the nearly degenerate Ψ_0 ($\langle\delta|M_{x'}|0\rangle \neq 0$) and $\Phi_1^{(1)}$ ($\langle\delta|M_{y'}|0\rangle \neq 0$) modes should appear in both fields $\mathbf{h}_1$ and $\mathbf{h}_2$. However, more precise THz measurements[15] have recently detected the low-frequency mode in both fields $\mathbf{h}_1$ and $\mathbf{h}_2$. At 4 K, Nagel *et al.*[15] even observed distinct low-frequency peaks at 2.03 and 2.26 meV. The observed threefold splitting of the 2.03 meV peak in a magnetic field may help to distinguish Ψ_0 and $\Phi_1^{(1)}$.

The spectroscopic intensities for $K = 0.0035$ meV and $S_0 = 0.015$ are summarized in Table I. These numerical results indicate that $\Psi_1^{(1)}$ and $\Psi_1^{(2)}$ should be the strongest of the four modes, in agreement with the THz results.[14,15] Surprisingly, Table I indicates that the intensity $I(\mathbf{h}_2)$ of $\Phi_2^{(1)}$ is roughly 5% that of $\Psi_1^{(1)}$. By contrast, recent THz measurements[15] indicate that $\Phi_2^{(1)}$ is only about 18% less intense than $\Psi_1^{(1)}$ in field $\mathbf{h}_2$. Whereas our model predicts that $\Psi_1^{(2)}$ is three times more intense than $\Psi_1^{(1)}$ in $\mathbf{h}_2$, recent measurements find only a factor of 1.4 between the two intensities. Most of these discrepancies can be explained by the dominance of one magnetic domain over the other two.

VI. INELASTIC NEUTRON-SCATTERING MEASUREMENTS

In earlier work[19] with $D' = 0$, we obtained conflicting estimates for the easy-axis anisotropy K based on the spectroscopic and neutron-scattering spectra. Because the instrumental resolution is broader than $4\pi\delta/a$,[9] inelastic neutron-scattering measurements at the AF Bragg point $(2\pi/a)[0.5,0.5,0.5]$ average over a range of $\mathbf{q}$ that includes both cycloidal satellites at $(2\pi/a)[0.5 \pm \delta, 0.5, 0.5 \mp \delta]$. For $D' = 0$, the spectroscopic mode frequencies indicated that $K \approx 0.002$ but the inelastic-scattering spectra indicated that $K \approx 0.004$.

We now reexamine the spectrum $\chi''(\omega)$ for $D' \neq 0$. The upper left-hand corner of Fig. 6 plots the measured spectrum.[9,19]

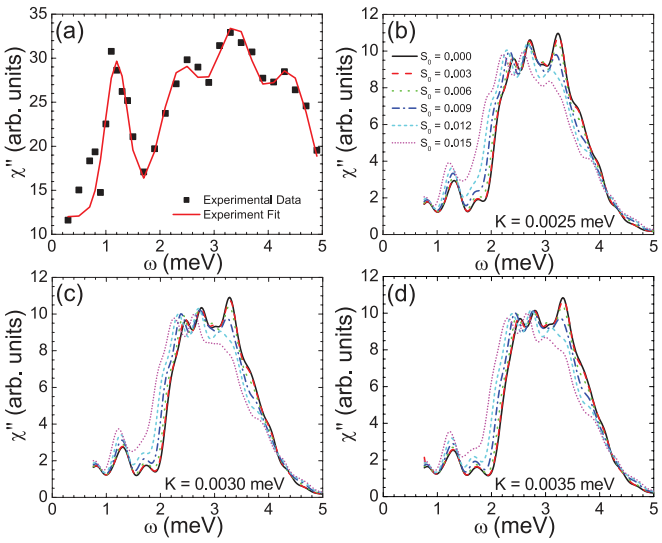

FIG. 6. (Color online) (a) The measured inelastic-scattering spectrum (Refs. 9,19) around $\eta = 0$ and the predicted spectrum for (b) $K =$ (b) 0.0025, (c) 0.003, and (d) 0.0035 meV with S_0 ranging from 0 to 0.015.

The resolution-averaged intensity spectrum is plotted versus ω in Figs. 6(b)–6(d) for three values of K and six values of S_0 from 0 to 0.015. The very low-frequency rise of $\chi''(\omega)$ due to Φ_0 at $\eta = \delta$ has been removed from both the measured and predicted spectra.

Below 5 meV, the measured $\chi''(\omega)$ contains four peaks at 1.2, 2.4, 3.4, and 4.4 meV. The peaks at 1.2 and 2.4 meV are primarily caused by $\Phi_1^{(1,2)}$ and Ψ_0. As shown in Fig. 4 for $S_0 = 0.015$, the separation between $\Phi_1^{(2)}$ and $\Phi_1^{(1)}/\Psi_0$ increases as K exceeds 0.001 meV. Correspondingly, the gap in the predicted spectrum centered at 2 meV widens with increasing K beyond 0.001 meV.

As shown in Fig. 5(b), $\Phi_1^{(2)}$ is slightly enhanced by S_0. But the resolution-averaged spectrum $\chi''(\omega)$ also involves nearby modes and shifts to lower frequencies with increasing S_0. For $S_0 = 0.015$ and $K = 0.0035$ meV, the low-frequency peak lies at 1.2 meV. So based on this single peak, $K \approx 0.0035$ meV provides good agreement with both the spectroscopic and inelastic measurements. Although its intensity increases with S_0 and it is more pronounced than in our previous work,[19] the predicted low-frequency peak at 1.2 meV is still considerably weaker than the measured peak.

For $K = 0.0035$ meV, the second peak lies at 2.5 meV when $S_0 = 0$ but shifts down to 2.3 meV when $S_0 = 0.015$. More problematically, the predicted spectrum contains three peaks between 2 and 4 meV (although the third peak is suppressed with S_0) whereas the measured spectrum contains only two. For $K = 0.0035$ meV and $S_0 = 0.015$, there are no predicted SW excitations between 4 and 5 meV at $\eta = 0$ or δ. Consequently, the observed peak at 4.4 meV is missing from our spectrum, which falls off much more rapidly than the measured $\chi''(\omega)$ above 4 meV. Keep in mind, however, that the predicted shape of $\chi''(\omega)$ sensitively depends on the resolution function used to perform the averaging.

VII. CONCLUSION

A primary motivation of this work was to see how well a microscopic model can describe the properties of one of the simplest and most technologically important multiferroic materials. We have demonstrated that all four modes observed by THz and Raman spectroscopies in $BiFeO_3$ are predicted by a model that includes two DM interactions, one along $\mathbf{y}'$ responsible for the cycloid periodicity and the other along $\mathbf{z}'$ responsible for its tilt of the cycloid out of the $x'z'$ plane. Using reasonable values for the easy-axis anisotropy and the DM interactions, we obtain excellent agreement with the measured mode frequencies. The parameters $D = 0.11$ meV, $D' = 0.054$ meV, and $K = 0.0035$ meV provide very good descriptions of both the spectroscopic and inelastic neutron-scattering measurements, thereby resolving an earlier disagreement.[19]

The spectroscopic modes evolve with the complexity of the cycloid. With a single DM interaction $\mathbf{D} = D\mathbf{y}'$, the cycloid is coplanar and purely harmonic. For nonzero frequencies, the only spectroscopically active mode is Ψ_1 ($\langle\delta|M_{x'}|0\rangle \neq 0$, $\langle\delta|M_{z'}|0\rangle \neq 0$), which coincides with the EM ($\langle\delta|P_{y'}^{\text{ind}}|0\rangle \neq 0$). Easy-axis anisotropy K along $\mathbf{z}'$ distorts the coplanar cycloid and introduces higher even harmonics

in the Hamiltonian H. The $2\mathbf{Q}$ potential splits $\Psi_{\pm1}$ into $\Psi_1^{(1)}$ ($\langle\delta|M_{x'}|0\rangle \neq 0$, $\langle\delta|P_{y'}^{\rm ind}|0\rangle \neq 0$) and $\Psi_1^{(2)}$ ($\langle\delta|M_{z'}|0\rangle \neq 0$); the $4\mathbf{Q}$ potential splits $\Phi_{\pm2}$ into $\Phi_2^{(1)}$ and $\Phi_2^{(2)}$. Hybridized with Φ_0 by the $2\mathbf{Q}$ potential, $\Phi_2^{(1)}$ ($\langle\delta|M_{y'}|0\rangle \neq 0$) becomes spectroscopically active. Finally, the DM interaction $\mathbf{D}' = D'\mathbf{z}'$ tilts the noncoplanar cycloid out of the $x'z'$ plane. Then Ψ_0 ($\langle\delta|M_{x'}|0\rangle \neq 0$) and $\Phi_1^{(1)}$ ($\langle\delta|M_{y'}|0\rangle \neq 0$) are dynamically and spectroscopically activated by their hybridization with $\Psi_1^{(1,2)}$ and Φ_0, respectively. Thus, additional interactions modify the mode spectrum as more modes hybridize with Φ_0 and $\Psi_1^{(1,2)}$.

Several experiments indicate that the low-temperature, low-field cycloid of $BiFeO_3$ undergoes a transition at about 140 K or 10 T. In THz measurements,[14] the low-frequency $\Psi_0/\Phi_1^{(1)}$ mode disappears above 120 K and the high-frequency $\Phi_2^{(1)}$ mode disappears above 150 K. Nevertheless, the selection rules governing the $\Psi_1^{(1,2)}$ modes do not change.[14] In Raman measurements, all modes persist for all temperatures but their frequencies[16] and intensities[17] display kinks at about 140 K. Optical[40] and electron-spin-resonance[41] measurements show anomalies at about 10 T with indications that the cycloidal phase above 10 T is the same as the one above 140 K. Recently, Nagel *et al.*[15] found that the THz modes exhibit kinks at about 5.5 T. But the nature of these transitions and the difference between the two cycloidal phases remain unknown.

Since D' is responsible for the low-frequency $\Psi_0/\Phi_1^{(1)}$ mode, a sudden change in D' at 140 K or 10 T would produce anomalies in its spectroscopic features. A jump in D' at 140 K would also produce a jump in the weak ferromagnetic moment $M_0(T)$. However, we do not understand the competing energies that would produce such a jump in D'. We hope that future experimental and theoretical work will resolve this and other mysteries surrounding $BiFeO_3$.

ACKNOWLEDGMENTS

We gratefully acknowledge conversations with Masaaki Matsuda, Jan Musfeldt, Satoshi Okamoto, and Toomas Rõõn. The research was sponsored by the US Department of Energy, Office of Basic Energy Sciences, Materials Sciences and Engineering Division (R.F.), by the Center for Integrated Nanotechnologies, a US Department of Energy, Office of Basic Energy Sciences user facility at Los Alamos National Laboratory, operated by Los Alamos National Security, LLC for the National Nuclear Security Administration of the US Department of Energy (J.T.H.), by Grants-in-Aid for Scientific Research from the Ministry of Education, Culture, and Technology, Japan (MEXT) (N.F.), and by the Max Planck Society (MPG), the Korea Ministry of Education, Science and Technology (MEST), Gyeongsangbuk-Do, and Pohang City (S.M.).

APPENDIX A: SW INTENSITIES

This section describes how to evaluate the SW intensities and eigenvectors $\underline{X}$, which are required in the next section to evaluate the spectroscopic matrix elements. The local reference frame for each spin $\mathbf{S}_i$ on site i is defined in terms of the unitary matrix $\underline{U}^i$ by $\bar{\mathbf{S}}_i = \underline{U}^i\,\mathbf{S}_i$. For spin

$$\mathbf{S} = S(\sin\theta\cos\phi, \sin\theta\sin\phi, \cos\theta), \tag{A1}$$

the matrices $\underline{U}$ and $\underline{U}^{-1}$ are given by

$$\underline{U} = \begin{pmatrix} \cos\theta\cos\phi & \cos\theta\sin\phi & -\sin\theta \\ -\sin\phi & \cos\phi & 0 \\ \sin\theta\cos\phi & \sin\theta\sin\phi & \cos\theta \end{pmatrix}, \tag{A2}$$

$$\underline{U}^{-1} = \begin{pmatrix} \cos\theta\cos\phi & -\sin\phi & \sin\theta\cos\phi \\ \cos\theta\sin\phi & \cos\phi & \sin\theta\sin\phi \\ -\sin\theta & 0 & \cos\theta \end{pmatrix}, \tag{A3}$$

so that $S\underline{U}^{-1}\cdot\mathbf{z} = \mathbf{S}$.

A Holstein-Primakoff transformation is used to express the local spin operators $\bar{\mathbf{S}}_i$ in terms of the bosons a_i and $a_i^\dagger$ with $\bar{S}_{iz} = S - a_i^\dagger a_i$, $\bar{S}_{i+} = \sqrt{2S}a_i$, and $\bar{S}_{i-} = \sqrt{2S}a_i^\dagger$. The Hamiltonian is then expanded in powers of $1/\sqrt{S}$ as $H = E_0 + H_1 + H_2 + \cdots$. While E_0 is the classical energy and H_1 must vanish,

$$H_2 = \sum_{\mathbf{q}} \mathbf{v}_{\mathbf{q}}^\dagger \cdot \underline{L}(\mathbf{q}) \cdot \mathbf{v}_{\mathbf{q}}, \tag{A4}$$

where $\mathbf{v}_{\mathbf{q}} = (a_{\mathbf{q}}^{(1)}, \ldots, a_{\mathbf{q}}^{(2M)}, a_{-\mathbf{q}}^{(1)\dagger}, \ldots, a_{-\mathbf{q}}^{(2M)\dagger})$ is a $4M$-dimensional vector and $\underline{L}(\mathbf{q})$ is a $4M$-dimensional matrix. Boson operators $a_{\mathbf{q}}^{(r)}$ with $1 \leqslant r \leqslant M = 222$ reside on layer 1 of the unit cell while those with $M+1 \leqslant r \leqslant 2M$ reside on layer 2. The sublattice index r refers to sites on either layer with $\mathbf{R}\cdot\mathbf{x}' = [r]a/\sqrt{2}$ where $[r] \equiv \mathrm{mod}(r, M)$.

Since $a_{\mathbf{q}}^{(r)}$ and $a_{\mathbf{q}}^{(r)\dagger}$ obey the commutation relations $[a_{\mathbf{q}}^{(r)}, a_{\mathbf{q}'}^{(s)\dagger}] = \delta_{r,s}\delta_{\mathbf{q},\mathbf{q}'}$ and $[a_{\mathbf{q}}^{(r)}, a_{\mathbf{q}'}^{(s)}] = 0$, $\mathbf{v}_{\mathbf{q}}$ and $\mathbf{v}_{\mathbf{q}}^\dagger$ satisfy the commutation relation $[\mathbf{v}_{\mathbf{q}}, \mathbf{v}_{\mathbf{q}'}^\dagger] = \underline{N}\delta_{\mathbf{q},\mathbf{q}'}$ where

$$\underline{N} = \begin{pmatrix} \underline{I} & 0 \\ 0 & -\underline{I} \end{pmatrix} \tag{A5}$$

and $\underline{I}$ is the $2M$-dimensional unit matrix.

A diagonal form for H_2 is given by

$$H_2 = \sum_{\mathbf{q}} \mathbf{w}_{\mathbf{q}}^\dagger \cdot \underline{L}'(\mathbf{q}) \cdot \mathbf{w}_{\mathbf{q}}, \tag{A6}$$

where $\mathbf{w}_{\mathbf{q}} = (\alpha_{\mathbf{q}}^{(1)}, \ldots, \alpha_{\mathbf{q}}^{(2M)}, \alpha_{-\mathbf{q}}^{(1)\dagger}, \ldots, \alpha_{-\mathbf{q}}^{(2M)\dagger})$ and the boson operators $\alpha_{\mathbf{q}}^{(n)}$ and $\alpha_{\mathbf{q}}^{(n)\dagger}$ also obey canonical commutation relations. The $4M$-dimensional matrix $\underline{L}'(\mathbf{q})$ is diagonal with real eigenvalues $\epsilon_n(\mathbf{q}) = \omega_n(\mathbf{q})/2 > 0$ ($n = 1, \ldots, 2M$) and $\epsilon_n(\mathbf{q}) = -\omega_n(\mathbf{q})/2 < 0$ ($n = 2M+1, \ldots, 4M$). So for each $\mathbf{q}$, there are $2M$ positive and $2M$ negative eigenvalues. The commutation relations yield

$$H_2 = \sum_{n,\,\mathbf{k}} \omega_n(\mathbf{q}) \left\{ \alpha_{\mathbf{q}}^{(n)\dagger}\alpha_{\mathbf{q}}^{(n)} + \frac{1}{2} \right\}, \tag{A7}$$

which identifies $\omega_n(\mathbf{q})$ as the SW frequency for mode n with wave vector $\mathbf{q}$.

The vectors $\mathbf{w}_{\mathbf{q}}$ and $\mathbf{v}_{\mathbf{q}}$ are related by $\mathbf{w}_{\mathbf{q}} = \underline{X}(\mathbf{q})\cdot\mathbf{v}_{\mathbf{q}}$ or $\mathbf{v}_{\mathbf{q}} = \underline{X}^{-1}(\mathbf{q})\cdot\mathbf{w}_{\mathbf{q}}$, where the $4M$-dimensional matrix $\underline{X}$ is normalized by $\underline{X}\cdot\underline{N}\cdot\underline{X}^\dagger = \underline{N}$. For fixed $\mathbf{q}$,

$$\sum_j [\mathcal{L}_{ij}(\mathbf{q}) - \delta_{ij}\epsilon_n(\mathbf{q})] X_{nj}^*(\mathbf{q}) = 0, \tag{A8}$$

where $\underline{\mathcal{L}}(\mathbf{q}) = \underline{L}(\mathbf{q}) \cdot \underline{N}$. The inverse $\underline{X}^{-1} = \underline{N} \cdot \underline{X}^{\dagger} \cdot \underline{N}$ is required to evaluate $\langle\delta|\mathbf{P}^{\rm ind}|0\rangle$ and $\langle\delta|\mathbf{M}|0\rangle$.

The wave vector $\mathbf{Q}$ and harmonic coefficients of the cycloid are obtained by minimizing E_0 using the "trial" spin state provided by Eqs. (2)–(4). If the spin angles on site r of layer 1 are θ_r and ϕ_r, then the angles on layers 1 and 2 are related by $\theta_{r+M} = \theta_r + \pi$ and $\phi_{r+M} = -\phi_r$. We assume that $\phi_r = \tau$ and $\phi_{r+M} = -\tau$ are independent of site position r on layers 1 and 2.

The spin-spin correlation function is defined by

$$S_{\alpha\beta}(\mathbf{q},\omega) = \frac{1}{2\pi N}\int dt\, e^{-i\omega t}\sum_{i,j} e^{-i\mathbf{q}\cdot(\mathbf{R}_i-\mathbf{R}_j)}\langle S_{i\alpha}(0)S_{j\beta}(t)\rangle = \sum_n \delta(\omega-\omega_n(\mathbf{q}))S^{(n)}_{\alpha\beta}(\mathbf{q}), \quad \text{(A9)}$$

where the final expression assumes that the SWs are undamped. The inelastic neutron-scattering cross section is[42]

$$S(\mathbf{q},\omega) = \sum_{\alpha,\beta}(\delta_{\alpha\beta} - q_\alpha q_\beta/q^2)S_{\alpha\beta}(\mathbf{q},\omega) = \sum_{n,\alpha}[1-(q_\alpha/q)^2]\delta(\omega-\omega_n(\mathbf{q}))S^{(n)}_{\alpha\alpha}(\mathbf{q}), \quad \text{(A10)}$$

which involves only the diagonal matrix elements of $S_{\alpha\beta}(\mathbf{q},\omega)$ (if there is a net moment, some off-diagonal matrix elements $\alpha \neq \beta$ are nonzero and antisymmetric). The diagonal SW intensities $S^{(n)}_{\alpha\alpha}(\mathbf{q})$ are given by

$$S^{(n)}_{\alpha\alpha}(\mathbf{q}) = \frac{S}{8M}\left|\sum_{r=1}^{2M} W^{(n)}_{r,\alpha}(\mathbf{q})\right|^2, \quad \text{(A11)}$$

where

$$W^{(n)}_{r,\alpha}(\mathbf{q}) = \left(U^{-1\,r}_{\alpha x} - iU^{-1\,r}_{\alpha y}\right)X^{-1}_{r,n+2M}(\mathbf{q}) + \left(U^{-1\,r}_{\alpha x} + iU^{-1\,r}_{\alpha y}\right)X^{-1}_{r+2M,n+2M}(\mathbf{q}). \quad \text{(A12)}$$

Even in the absence of damping, the instrumental resolution will broaden the δ functions in $S(\mathbf{q},\omega)$ in Eq. (A10). The magnetic form factor for Fe^{3+} should also be included in $S(\mathbf{q},\omega)$.

APPENDIX B: SPECTROSCOPIC MATRIX ELEMENTS

This section evaluates the matrix elements for the induced electric polarization $\mathbf{P}^{\rm ind}$ and the magnetic moment $\mathbf{M}$ between the ground state $|0\rangle$ and an excited state $|\delta\rangle$ with a single magnon at the cycloidal wave vector $\mathbf{Q}$.

Since $P^{\rm ind}_{x'} = 0$, only the y' and z' components are considered. Expanded about equilibrium, $P^{\rm ind}_{y'}$ becomes

$$P^{\rm ind}_{y'} = \lambda S\Bigg\{\sum_{r=1}^{M}\sin\theta_r\cos\phi_r\,[-S_{[r+2],y'} + S_{[r-2],y'} + S_{[r+2]+M,y'} - S_{[r-2]+M,y'}] + \sum_{r=1}^{M}\sin\theta_r\sin\phi_r\,[S_{[r+2],x'} - S_{[r-2],x'} + S_{[r+2]+M,x'} - S_{[r-2]+M,x'}]\Bigg\}. \quad \text{(B1)}$$

After some work, we obtain the EM matrix element y' for SW mode n:

$$\begin{aligned}\langle\delta|P^{\rm ind}_{y'}|0\rangle = \lambda S\sqrt{\frac{S}{2}}\sum_{r=1}^{M}\sin\theta_r\, e^{iq_0ar}\Big\{&[\cos\theta_{[r+2]}\sin(\phi_r-\phi_{[r+2]}) + i\cos(\phi_r-\phi_{[r+2]})]\left(X^{-1}_{[r+2],n+2M} - X^{-1}_{[r+2]+M,n+2M}\right)e^{2iq_0a}\\ &+[\cos\theta_{[r+2]}\sin(\phi_r-\phi_{[r+2]}) - i\cos(\phi_r-\phi_{[r+2]})]\left(X^{-1}_{[r+2]+2M,n+2M} - X^{-1}_{[r+2]+3M,n+2M}\right)e^{2iq_0a}\\ &-[\cos\theta_{[r-2]}\sin(\phi_r-\phi_{[r-2]}) + i\cos(\phi_r-\phi_{[r-2]})]\left(X^{-1}_{[r-2],n+2M} - X^{-1}_{[r-2]+M,n+2M}\right)e^{-2iq_0a}\\ &-[\cos\theta_{[r-2]}\sin(\phi_r-\phi_{[r-2]}) - i\cos(\phi_r-\phi_{[r-2]})]\left(X^{-1}_{[r-2]+2M,n+2M} - X^{-1}_{[r-2]+3M,n+2M}\right)e^{-2iq_0a}\Big\},\end{aligned} \quad \text{(B2)}$$

where $q_0 = 2\pi\delta/a$.

Similarly, $P^{\rm ind}_{z'}$ can be expanded as

$$P^{\rm ind}_{z'} = \lambda S\Bigg\{\sum_{r=1}^{M}\cos\theta_r\,[S_{[r+2],x'} - S_{[r-2],x'} - S_{[r+2]+M,x'} + S_{[r-2]+M,x'}] - \sum_{r=1}^{M}\sin\theta_r\cos\phi_r\,[S_{[r+2],z'} - S_{[r-2],z'} - S_{[r+2]+M,z'} + S_{[r-2]+M,z'}]\Bigg\}. \quad \text{(B3)}$$

The EM matrix element z' for SW mode n is

$$\begin{aligned}\langle\delta|P^{\rm ind}_{z'}|0\rangle = \lambda S\sqrt{\frac{S}{2}}\sum_{r=1}^{M}e^{iq_0ar}\Big\{&[g_{r,[r+2]} + i\cos\theta_r\sin\phi_{[r+2]}]\left(X^{-1}_{[r+2],n+2M} - X^{-1}_{[r+2]+M,n+2M}\right)e^{2iq_0a}\\ &+[g_{r,[r+2]} - i\cos\theta_r\sin\phi_{[r+2]}]\left(X^{-1}_{[r+2]+2M,n+2M} - X^{-1}_{[r+2]+3M,n+2M}\right)e^{2iq_0a}\\ &-[g_{r,[r-2]} + i\cos\theta_r\sin\phi_{[r+2]}]\left(X^{-1}_{[r-2],n+2M} - X^{-1}_{[r-2]+M,n+2M}\right)e^{-2iq_0a}\\ &-[g_{r,[r+2]} - i\cos\theta_r\sin\phi_{[r-2]}]\left(X^{-1}_{[r-2]+2M,n+2M} - X^{-1}_{[r-2]+3M,n+2M}\right)e^{-2iq_0a}\Big\},\end{aligned} \quad \text{(B4)}$$

where

$$g_{r,s} = \cos\theta_r \cos\theta_s \cos\phi_s + \sin\theta_r \sin\theta_s \cos\phi_r. \quad \text{(B5)}$$

For $K = 0.0035$ meV and $S_0 = 0.015$, Φ_0 has the small matrix element $\langle\delta|P^{\rm ind}_{z'}|0\rangle \approx 0.19$, about 60 times smaller than $\langle\delta|P^{\rm ind}_{y'}|0\rangle \approx 12.2$ for $\Psi^{(1)}_1$.

The MR matrix element for SW mode n is much more simply given by

$$\langle\delta|M_\alpha|0\rangle = \sqrt{2S}\mu_B \sum_{r=1}^{2M} e^{iq_0a[r]}\mathrm{sgn}(M - r + 1/2)\, W^{(n)}_{r,\alpha}(\mathbf{Q}), \quad \text{(B6)}$$

which uses

$$e^{i\mathbf{Q}\cdot\mathbf{R}} = e^{iq_0a[r]}\,\mathrm{sgn}(M - r + 1/2). \quad \text{(B7)}$$

Notice that $W^{(n)}_{r,\alpha}(\mathbf{q})$ also enters the SW intensity $S^{(n)}_{\alpha\alpha}(\mathbf{q})$ of Eq. (A11). While the SW intensity $S^{(n)}_{\alpha\alpha}(\mathbf{Q})$ is proportional to the amplitude squared of the sum of $W^{(n)}_{r,\alpha}(\mathbf{Q})$ over r, the matrix element $\langle\delta|M_\alpha|0\rangle$ is proportional to the Fourier transform of $W^{(n)}_{r,\alpha}(\mathbf{Q})$ over r.

[1] W. Eerenstein, N. D. Mathur, and J. F. Scott, Nature (London) **442**, 759 (2006).

[2] J. R. Teague, R. Gerson, and W. J. James, Solid State Commun. **8**, 1073 (1970).

[3] I. Sosnowska, T. Peterlin-Neumaier, and E. Steichele, J. Phys. C **15**, 4835 (1982).

[4] D. Lebeugle, D. Colson, A. Forget, M. Viret, A. M. Bataille, and A. Goukasov, Phys. Rev. Lett. **100**, 227602 (2008).

[5] S. Lee, W. M. Ratcliff II, S.-W. Cheong, and V. Kiryukhin, Appl. Phys. Lett. **92**, 192906 (2008).

[6] J. Park, S.-H. Lee, S. Lee, F. Gozzo, H. Kimura, Y. Noda, Y. J. Choi, V. Kiryukhin, S.-W. Cheong, Y. Jo, E. S. Choi, L. Balicas, G. S. Jeon, and J.-G. Park, J. Phys. Soc. Jpn. **80**, 114714 (2011).

[7] S. Lee, T. Choi, W. Ratcliff, R. Erwin, S.-W. Cheong, and V. Kiryukhin, Phys. Rev. B **78**, 100101(R) (2008).

[8] J. Jeong, E. A. Goremychkin, T. Guidi, K. Nakajima, G. S. Jeon, S.-A. Kim, S. Furukawa, Y. B. Kim, S. Lee, V. Kiryukhin, S.-W. Cheong, and J.-G. Park, Phys. Rev. Lett. **108**, 077202 (2012).

[9] M. Matsuda, R. S. Fishman, T. Hong, C. H. Lee, T. Ushiyama, Y. Yanagisawa, Y. Tomioka, and T. Ito, Phys. Rev. Lett. **109**, 067205 (2012).

[10] To account for the suppression of the observed moment at 200 K, the authors of Ref. 9 took $2\mu_B\sqrt{S(S+1)} = 4.11\mu_B$ to be about 30% lower than its value with $S = 5/2$. Here we take $2\mu_B\sqrt{S(S+1)} = 5.92\mu_B$ and reduce the exchange interactions accordingly. So the estimates $J_1 = 6.48$ meV, $J_2 = 0.29$ meV, and $D = 0.162$ meV from Ref. 9 are equivalent to $J_1 = -4.5$ meV, $J_2 = -0.2$ meV, and $D = 0.119$ meV in this paper. All spectroscopic frequencies are measured at or extrapolated to 200 K.

[11] M. Ramazanoglu, W. Ratcliff, Y. J. Choi, S. Lee, S.-W. Cheong, and V. Kiryukhin, Phys. Rev. B **83**, 174434 (2011).

[12] J. Herrero-Albillos, G. Catalan, J. A. Rodriguez-Velamazan, M. Viret, D. Colson, and J. F. Scott, J. Phys.: Condens. Matter **22**, 256001 (2010).

[13] I. Sosnowska and R. Przenioslo, Phys. Rev. B **84**, 144404 (2011).

[14] D. Talbayev, S. A. Trugman, S. Lee, H. T. Yi, S.-W. Cheong, and A. J. Taylor, Phys. Rev. B **83**, 094403 (2011).

[15] U. Nagel, T. Katuwal, H. Engelkamp, D. Talbayev, H. T. Yi, S.-W. Cheong, and T. Rõõm, arXiv:1302.2491.

[16] M. Cazayous, Y. Gallais, A. Sacuto, R. de Sousa, D. Lebeugle, and D. Colson, Phys. Rev. Lett. **101**, 037601 (2008).

[17] M. K. Singh, R. S. Katiyar, and J. F. Scott, J. Phys.: Condens. Matter **20**, 252203 (2008); J. F. Scott, M. K. Singh, and R. S. Katiyar, *ibid.* **20**, 322203 (2008).

[18] P. Rovillain, M. Cazayous, Y. Gallais, A. Sacuto, R. P. S. M. Lobo, D. Lebeugle, and D. Colson, Phys. Rev. B **79**, 180411(R) (2009).

[19] R. S. Fishman, N. Furukawa, J. T. Haraldsen, M. Matsuda, and S. Miyahara, Phys. Rev. B **86**, 220402(R) (2012).

[20] I. Sosnowska and A. K. Zvezdin, J. Magn. Magn. Mater. **140–144**, 167 (1995).

[21] A. M. Kadomtseva, A. K. Zvezdin, Yu.F. Popv, A. P. Pyatakov, and G. P. Vorob'ev, JETP Lett. **79**, 571 (2004).

[22] C. Ederer and N. A. Spaldin, Phys. Rev. B **71**, 060401(R) (2005).

[23] A. P. Pyatakov and A. K. Zvezdin, Eur. Phys. J. B **71**, 419 (2009).

[24] K. Ohoyama, S. Lee, S. Yoshii, Y. Narumi, T. Morioka, H. Nojiri, G. S. Jeon, S.-W. Cheong, and J.-G. Park, J. Phys. Soc. Jpn. **80**, 125001 (2011).

[25] M. Tokunaga, M. Azuma, and Y. Shimakawa, J. Phys. Soc. Jpn. **79**, 064713 (2010).

[26] M. Ramazanoglu, M. Laver, W. Ratcliff, S. M. Watson, W. C. Chen, A. Jackson, K. Kothapalli, S. Lee, S.-W. Cheong, and V. Kiryukhin, Phys. Rev. Lett. **107**, 207206 (2011).

[27] P. Chen, Ö. Günaydın-Sen, W. J. Ren, Z. Qin, T. V. Brinzari, S. McGill, S.-W. Cheong, and J. L. Musfeldt, Phys. Rev. B **86**, 014407 (2012).

[28] F. Bai, J. Wang, M. Wuttig, J. F. Li, N. Wang, A. P. Pyatakov, A. K. Zvezdin, L. E. Cross, and D. Viehland, Appl. Phys. Lett. **86**, 032511 (2005).

[29] M. E. Zhitomirsky and I. A. Zaliznyak, Phys. Rev. B **53**, 3428 (1996).

[30] R. S. Fishman and S. Okamoto, Phys. Rev. B **81**, 020402(R) (2010).

[31] J. T. Haraldsen and R. S. Fishman, J. Phys.: Condens. Matter **21**, 216001 (2009).

[32] R. de Sousa and J. E. Moore, Phys. Rev. B **77**, 012406 (2008).

[33] H. Katsura, N. Nagaosa, and A. V. Balatsky, Phys. Rev. Lett. **95**, 057205 (2005).

[34] M. Mostovoy, Phys. Rev. Lett. **96**, 067601 (2006).

[35] I. A. Sergienko and E. Dagotto, Phys. Rev. B **73**, 094434 (2006).

[36] Φ_0 is not strictly a Goldstone mode because rotational invariance about $\mathbf{z}'$ is broken by $\mathbf{D}$. However, the energy gap is so small that we are unable to reliably estimate its size.

[37] A. V. Zalesskii, A. K. Zvezdin, A. A. Frolov, and A. A. Bush, JETP Lett. **71**, 465 (2000); A. V. Zalesskii, A. A. Frolov, A. K. Zvezdin, A. A. Gippius, E. N. Morozova, D. F. Khozeev, A. S. Bush, and V. S. Pokatilov, JETP **95**, 101 (2002).

[38]S. Pokatilov and A. S. Sigov, JETP **110**, 440 (2010).
[39]S. Miyahara and N. Furukawa, J. Phys. Soc. Jpn. **81**, 023712 (2012).
[40]X. S. Xu, T. V. Brinzari, S. Lee, Y. H. Chu, L. W. Martin, A. Kumar, S. McGill, R. C. Rai, R. Ramesh, V. Gopalan, S.-W. Cheong, and J. L. Musfeldt, Phys. Rev. B **79**, 134425 (2009).
[41]B. Ruette, S. Zvyagin, A. P. Pyatakov, A. Bush, J. F. Li, V. I. Belotelov, A. K. Zvezdin, and D. Viehland, Phys. Rev. B **69**, 064114 (2004).
[42]G. Shirane, S. M. Shapiro, and J. M. Tranquada, *Neutron Scattering with a Triple-Axis Spectrometer* (Cambridge University Press, Cambridge, UK, 2004).